Photo-Hall-Effect Spectroscopy with Enhanced Illumination in p-Cd$_{1-x}$Mn$_x$Te Showing Negative Differential Photoconductivity

A. Musiienko,[1,][*] R. Grill,[1] P. Moravec,[1] P. Fochuk,[2] I. Vasylchenko,[1] H. Elhadidy,[3,4] and L. Šedivý[1]

[1]*Institute of Physics, Charles University, Prague 121 16, Czech Republic*
[2]*Chernivtsi National University, Ukraine*
[3]*Central European Institute of Technology, Institute of Physics of Materials, ASCR, Brno 61662, Czech Republic*
[4]*Faculty of Science, Physics Department, Mansoura University, Mansoura 35516, Egypt*

The charge-transport properties of semiconductor and semiinsulator materials are strongly controlled by the crystallographic defects manifesting energy states in the bandgap. In this paper, we study deep levels (DLs) in p-type Cd$_{1-x}$Mn$_x$Te by photo-Hall-effect spectroscopy with enhanced illumination. We show that the mobility of minority (925 ± 11 cm^2 s^{-1} V^{-1}) and majority (59.6 ± 0.4 cm^2 s^{-1} V^{-1}) carriers can be deduced directly from the spectra by using proper wavelength and excitation intensity. Four deep levels with ionization energies $E_{t1} = E_V + 0.63$ eV, $E_{t2} = E_V + 0.9$ eV, $E_{t3} = E_C - 1.0$ eV, and $E_{t4} = E_C - 1.3$ eV are detected and their positions in the bandgap are verified by comparison of photogenerated electron and hole concentrations. The deduced DL model is analyzed by numerical simulations with Shockley-Reed-Hall charge generation-recombination theory and compared with alternative DL models differing in the position of selected DLs relative to E_C and E_V. We show that the consistent explanation of collected experimental data principally limits the applicability of alternative DL models. We also demonstrate the importance of the extended operation photon fluxes ($I > 4 \times 10^{14}$ cm^{-2} s^{-1}) used in the spectra acquisition for correct determination of DL character. Negative differential photoconductivity is observed and studied by charge dynamic theoretical simulations.

I. INTRODUCTION

Inevitable crystallographic defects such as point, line, planar, and bulk defects represent one of the most serious problems currently faced by a semiconductor manufacture technology. The presence of such defects in the semiconductor lattice leads to the formation of energy states in the bandgap. These states can be divided into two major groups. The first one, shallow levels, consists of less localized states with activation energies E_t typically less or similar to the thermal energy kT. Shallow states are produced by small lattice perturbations and generally act as dopants (donors or acceptors) without a harmful influence on the material. The second group is called deep levels (DLs), with E_t significantly exceeding kT. The difference from the previous case of shallow states consists in much larger perturbation brought by these defects to the lattice potential in the close vicinity of the defect. Thus, the wave function of the trapped electron (or hole) is much more localized. Deep levels have a harmful impact on the utilization of the semiconductor in optoelectronic applications acting as electron (hole) traps or recombination centers depending on the

ratio of their cross sections σ_e/σ_h, where σ_e (σ_h) is the electron (hole) capture cross section. Many different deep-level spectroscopy methods [1–4] can identify deep-level ionization energy but a common problem is identifying the relative DL position inside the bandgap, i.e., whether DL energy locates below or above the Fermi energy. Knowledge of the exact DL position in the bandgap and its trapping characteristics plays a crucial role in the semiconductor characterization [5]. Multiple achievements were attained by photo-Hall-effect spectroscopy (PHES). It was used to prove the bipolar character of photoconduction in high-resistivity p-CdTe:Cl [6]. Low-temperature (10–40 K) PHES was successfully used for the characterization of impurities in p-HgCdTe [7]. A phenomenological model of deep donors in GaSb:S was developed and supported by PHES [8,9]. The character of DLs was revealed in semiinsulating GaAs, where all identified traps were found to be electron-type [10]. Another approach to measure the mobility of photocarriers by polarization-sensitive terahertz emission in the magnetic field was presented by Lin *et al.* [11]. It was found by Chen *et al.* [12,13] that PHES can be used for characterizing hybrid organic-inorganic lead CH$_3$NH$_3$PbCl$_3$(Br$_3$ or I$_3$) perovskites. PHES measurements in materials with low carrier mobility or suppressed Hall signal [14] can be used with a combination of

———————
[*]Corresponding author. musienko.art@gmail.com

the alternating magnetic field and lock-in amplifier [13]. In such a setup, the magnetic signal is chosen as the reference signal. Majority and minority carrier mobilities are important material parameters for many semiconductor devices such as solar cells, radiation detectors, diodes, transistors, etc. While the majority carrier mobility can be obtained by several techniques [5,15,16], the minority carrier mobility is hardly accessible.

The PHES measurements can be divided into two groups: the Hall signal measurements as a function of illumination intensity at various temperatures and the Hall signal measurements with different illuminating photon energies. Some modifications of the experiment are possible inside the groups, such as dual-photon energy illumination [17], or time transient measurements [18]. In our previous research [18], we pointed out that PHES faces a serious problem in the p-type material where strong recombination of minority carriers (electrons) suppresses electron impact in Hall mobility (μ_H) and photoconductivity (PhC). We also showed that the determination of DL position in the bandgap for n-type CdZnTe is complicated and can be accessed in the dual-wavelength illumination regime [17]. Because of these limitations, scant interest was given to PHES by researchers and the benefits of the method were underrated.

Negative differential photoconductivity (NDPC) is often observed in optical transport measurements of semiconductors. It is characterized by a decrease of the photoconductivity under enhanced illumination [19]. The effect of the conductivity decrease under illumination below the dark equilibrium value is known as absolute negative photoconductivity (ANPC) [20]. According to known models, NDPC and ANPC can be induced by two mechanisms. The first one is associated with a decrease in the carrier mobility induced by light radiation. This effect can be reached by stimulation of scattering mechanisms as shown for graphene [11,21], gold nanoparticles [22], Ge(Si) type-II quantum dots [23], and interacting quantum gas [24]. NDPC stimulated by potential nonuniformity was observed by our group in CdZnTe [17] and by Shalish *et al.* [25] in GaAs films using Hall photovoltage. The second mechanism producing NDPC is the decrease of the majority carrier concentration due to recombination of minority carriers supported by a recombination-type crystallographic defect. This model was first proposed by Stockmann [26] and implemented for diamond photodetectors [20], thin films [27], MoS$_2$ monolayers [28], p-type PbEuTe, and other materials. A similar mechanism of the enhanced radioactive capture of hot electrons was proposed by Ridley [29] for III-V and II-VI semiconductors. Despite a large number of experimental observations, the detailed theoretical study of NDPC (or ANPC) induced by defect levels was not presented. A simple model was given for inhomogeneous materials by Bube [30]. Despite the similar nature of the two effects, the connection between

NDPC and ANPC was not shown. The dependence of NDPC on DL parameters was also not specified.

The binary compound semiconductor CdTe and its ternary modifications Cd$_{1-x}$Zn$_x$Te and Cd$_{1-x}$Mn$_x$Te have a lot of applications in x- and gamma-ray detection [31,32] and in photovoltaics [33] due to a convenient tunable bandgap and good absorption properties [34]. Despite these benefits, as grown materials often suffer from crystallographic defects that deteriorate the transport properties of the devices [35]. The CdTe-based material resistivity homogeneity and detection properties can be enhanced by adding Se or Mn into the solution [36,37] due to uniform segregation of these components. Moreover, the bandgap energy can be controlled by the compound composition [38]. Such compound materials have known limitations for detector applications, such as strong carrier recombination [39] and device polarization [40,41] caused by deep levels inside the bandgap.

In this study, we combine the PHES measured at tunable illumination intensity and photon energy and characterize p-Cd$_{1-x}$Mn$_x$Te single crystal revealing NDPC. Experimental results are analyzed with the Shockley-Read-Hall (SRH) model and the DL structure is found. The suppressed electron signal is overcome by using a more powerful white laser source. We argue that such innovation strongly upgrades PHES capabilities, especially for semiinsulating semiconductors, such as GaAs, InP, HgI$_2$, TlBr, PbI$_2$, SiC, CdTe-based materials, CH$_3$NH$_3$PbCl$_3$(Br$_3$ or I$_3$) perovskites, and also for organic semiconductors where the properties of both majority and minority carriers may be determined. We demonstrate the possibility to disclose both minority and majority carrier mobilities using the Hall mobility measured as a function of illumination intensity at certain photon energy $h\nu$ (obtained from PHES spectra) and intensity where hole or electron generation predominates. Using photo-Hall-effect measurements and Shockley-Read-Hall charge kinetic simulations, we show the reason for NDPC and ANPC appearance as well as the dependence of these effects on DL parameters, such as carrier capture cross sections, photon capture cross sections, and DL concentration. We also demonstrate that NDPC can be a sign of bad transport properties as it may lead to the suppression of free-carrier generation especially at a high-flux illumination.

II. EXPERIMENT

A. Material

To show the principles of the PHES method, the p-Cd$_{1-x}$Mn$_x$Te sample is chosen. The single crystal is grown at the Chernivtsii National University by the vertical gradient freezing method with Mn content of 10%. The sample is cut from a wafer by a diamond saw and polished on an alumina powder with 1 μm grain size. Afterwards, each side is chemomechanically polished for 30 s in 3%

bromine-ethylene glycol solution [42,43]. Finally, bars adopted for the classical galvanomagnetic measurement are etched in 2% bromine-methanol solution for 1 min. After each chemical treatment, the sample is rinsed with methanol and acetone.

Gold contacts for measurements are electrolessly deposited [44] on a premasked surface in 1% aqueous $AuCl_3$ solution. Resulting samples are rinsed in water and cleaned with acetone. The Fermi energy $E_F = E_V + 0.62$ eV found from the dark-hole concentration is consistent with the given p-type resistivity of 3×10^8 Ω cm. The bandgap energy of the material is $E_g = 1.62$ eV at room temperature for the given Mn content [38]. The laser-induced current technique shows no hole or electron transient signal in this sample.

B. Photo-Hall-effect measurements

The principle of PHES is depicted in Fig. 1. A bar-like p-type sample with dimensions of $2 \times 3 \times 12$ mm^3 is used in the classical six-contact Hall-bar shape convenient for galvanomagnetic measurements. Measurements are performed at room temperature with a constant magnetic field B of 1 T. The longitudinal voltage V, the current I, and the transverse Hall voltage V_H are measured directly from the experiment. The conductivity $cond$, Hall coefficient R_H, and the Hall mobility μ_H are obtained by the following relations:
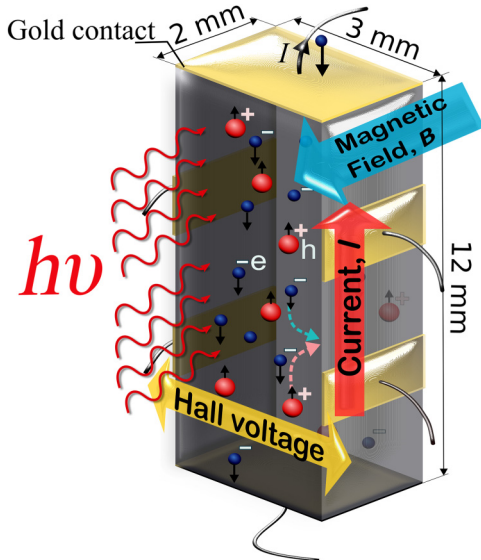
$$cond = \frac{IL}{VS}, \qquad (1)$$

FIG. 1. Basic principles of the PHES method. The monochromatic illumination stimulates the free-carrier generation. Photogenerated carriers are affected by Lorenz force and the electric field lengthwise the sample. The Hall voltage can be found under the steady-state conditions.

$$R_H = \frac{V_H d}{IB}, \qquad (2)$$

$$\mu_H = cond \times R_H = \frac{L}{SV}\frac{V_H d}{B}, \qquad (3)$$

where S, L, and d are the cross section, distance between conductivity probes, and thickness of the sample, respectively. Note that the obtained value of μ_H is determined by the V_H:V ratio. Therefore, μ_H remains unaffected by the contingent transversal inhomogeneity of the sample induced, for example, by surface leakage current, if the purely p-type character and spatially constant carrier mobility coextend through the whole sample. The small injection conditions are satisfied for all measurements, and the sample showed linear current-voltage characteristics. We also study the influence of the illumination on Au contacts, and we ascertain that the photovoltage is much less than the characteristic Hall voltage measured in PHES. For the right interpretation of PHES data, the influence of the surface charge should be assessed. Let us consider two principal disturbances introduced to the PHES data by the surface.

1. It is known that surface leakage current affects the apparent conductivity of high-resistivity semiconductors if it is determined by the simple two-probe method. The bulk current and surface leakage current cannot be distinguished in such a setup [45]. A similar shortcoming also appears in the PHES measured on the Hall-bar sample. Consequently, the determined dark conductivity results larger than the real dark bulk conductivity, which directly impairs the precision of E_F evaluated from these data. Considering surface leakage current, determined Fermi energy could be moved further from E_v by tens of meV. In Sec. IV B, we discuss further the consequences of such a E_F deviation on the DL properties evaluated with the suggested model.

2. In addition to the surface leakage current, one should also consider the dissimilar structural and optical properties of the bulk and surface that could affect the PHES data. Estimating the characteristic density of deep states localized near E_F similar to approximately 10^{12} cm^{-3} and band bending at the surface of 0.2 eV, we derive the thickness of the depleted layer using a well-known formula [46] as 10 μm, i.e., much less than our sample dimensions ($2 \times 3 \times 12$ mm^3). Such a thin layer does not contribute markedly to the light absorption below the bandgap energy where the joint density of states is very low and the absorption coefficient decreases below 1 cm^{-1} [34]. Increasing hv close to or above E_g, we observe at first an enhanced carrier generation when most of the photons are absorbed in the bulk. In contrast, further growth of hv induces the light absorption near the surface where the carriers intensely recombine via surface recombination and the detected photocarrier density and photoconductivity are suppressed. Such a feature is clearly visible in the

PHES spectra, see, e.g., [18] or Fig. 4, where the photo-conductivity for $hv > 1.6$ eV decreases. PHES signal could also be worsened by a significant distortion of the surface caused by improper surface treatment or even by formation of a second phase on the surface. Similar abnormalities could induce parasitic transitions erroneously assigned to the bulk material. The appearance of such a heterogeneous structure would, however, result in an increase of photo-voltage, which is very low in our sample. The surface treatment is performed with care by the procedure described in Sec. II A, which is used as a common approach for sample preparation. We thus conclude that PHES data are not violated by the surface depletion layer in our sample.

Summarizing, the charge transport in the surface depletion layer may affect especially dark electric properties of high-resistivity samples where the surface conduction is similar or exceeds the bulk conduction and consequently E_F could be burdened by some error. The sub-bandgap photoexcitation conveniently amplifies the bulk transport and leaves the effect of the surface low.

In our previous contribution [18], the moderate photon flux emitted by a conventional lamp source (halogen or mercury) filtered by a monochromator (the common output flux $<10^{14}$ cm^{-2} s^{-1}) did not allow for sufficient minority carrier generation in the energy region below the Urbach tail. To overcome this obstacle we upgrade the equipment and use a more powerful white laser with a maximal fil-tered output photon flux of 1.3×10^{15} cm^{-2} s^{-1}. The laser source provides nearly constant photon flux in the 0.6–1.4 eV energy region [47], which is in the strongest interest for DL spectroscopy. The sharp rise of the laser intensity near 1090 nm (25 nm segment) [47] is skipped by a monochro-mator. The spectral resolution of the monochromator is measured using an Ocean Optics spectrometer. The resolu-tion (defined by FWHM) grows nearly linearly from 0.01 eV at 0.5 eV up to 0.11 eV at 1.3 eV. Linear interpola-tion of these values is used to correctly determine the DL threshold energies at intermediate energies.

The decrease of conductivity is not observed on other semiinsulating samples without NDPC in a similar energy region. To track the evolution of the photo Hall signal under illumination intensity, we measure spectra at three different constant photon fluxes. For the study of carrier properties at higher illumination flux, we also use 0.95 and 1.46 eV laser diodes with the maximal photon flux of 1.2×10^{16} and 3×10^{17} cm^{-2} s^{-1}, respectively.

III. THEORY

A. The bipolar conduction and the interpretation concept of photo-Hall-effect data

Overall in this paper we assume a homogeneous sample with space-independent carrier density and mobility both in the dark and under illumination. The transverse Hall voltage and longitudinal conductivity in the dark in p-type material depend on the dark minority (n_0) and majority (p_0) carrier concentrations and their mobilities. Dark car-rier concentrations are further adjusted by photogenerated holes $p = p_0 + \Delta p$ and electrons $n = n_0 + \Delta n$ after illumi-nation of the sample. It is important to note that $\Delta n \neq \Delta p$ and corresponding values mainly depend on filling of DLs in the bandgap, illumination photon energy, and intensity. In the case of ANPC, Δn or Δp may even be negative. The bipolar conductivity *cond*, Hall coefficient R_H, photo-conductivity PhC, and Hall mobility μ_H are related to the free electron n and hole p concentrations by the relations

$$cond = q_e(\mu_h p + \mu_e n), \tag{4}$$

$$R_H = \frac{\mu_h^2 p - \mu_e^2 n}{q_e(\mu_h p + \mu_e n)^2}, \tag{5}$$

$$\text{PhC} = q_e(\mu_h \Delta p + \mu_e \Delta n), \tag{6}$$

$$\mu_H = \frac{\left| \mu_h^2 p - \mu_e^2 n \right|}{\mu_h p + \mu_e n}, \tag{7}$$

where q_e, μ_e, and μ_h are an elementary charge, and electron and hole mobility, respectively. Whenever the illumination photon energy (hv) reaches the trap energy counted relative to respective band, free electrons or holes are generated. This leads to a change of the spectral envelope and a rise of conductivity. In the case of p-CdMnTe, the response of μ_H to the photogenerated holes manifests in the fixation of the p-type character of the material often accompanied by an increase of μ_H, see Eq. (7). This μ_H enhancement is interpreted as a result of screening of charge impurity scattering and smoothing of potential fluctuations. On the other hand, photogenerated electrons provide a decrease of μ_H until the sign reversal of V_H arises at $n = (\mu_h/\mu_e)^2 p$, which may be well approximated by $n \approx 0.01p$ for CdTe-based compound materials. It is important to note here that whilst positive V_H proves the p-type character of the mate-rial, due to the higher electron mobility, the negative V_H does not directly testify to the n-type. The comparison of μ_e and μ_H must be included to solve this task.

Analyzing μ_H as a function of photon energy and light intensity enables us to determine the position of the DLs inside the bandgap. Due to the higher electron mobility, an even smaller rise of electron concentration caused by secondary electron emission from the DL with threshold energy $E_t > E_F$, outlined by DL model No. 2 in Fig. 2, might produce the μ_H decrease. The secondary emis-sion involves thermal detrapping and secondary photon-induced transition ($E_g - hv$) to the conduction band. A smart treatment must, therefore, be chosen for the res-olution of this task. The solution of the problem stems from different mechanisms of free-electron generation. The photon-induced transition from the filled DL local-ized below E_F to the conduction band satisfies the rule

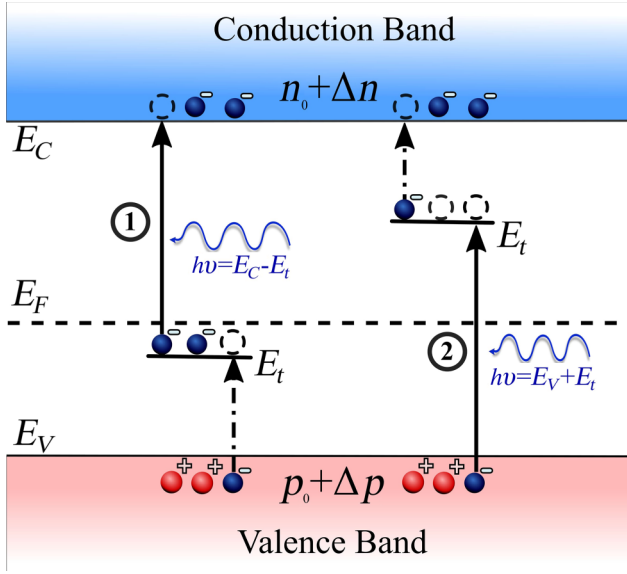FIG. 2. Competing deep-level models No. 1 and No. 2. Solid and dashed arrows show direct and secondary carrier generation processes correspondingly. E_F shows the Fermi level position in p-type material.

$\Delta n = \Delta n_t^{empt} + \Delta p$, where Δn_t^{empt} is a concentration of photo-induced empty states of the deep level (see Fig. 2, model No. 1). The secondary electron emission produced by empty (or nearly empty) DL with the energy $E_t > E_F$ (model No. 2) is ruled by a similar relation $\Delta n + \Delta n_t = \Delta p$, where Δn_t is a concentration of trapped electrons on the deep level. As we can see, this alternative transition is followed by predominant hole generation and the photogenerated hole concentration must be higher than the concentration of photogenerated electrons, i.e., $\Delta p > \Delta n$. Comparing Δp and Δn may allow us to distinguish both models. As Δp and Δn cannot be determined directly in a single experiment, detailed numerical simulation of charge dynamics in the photoexcited system is applied to prove the DL allocation. In the case of multiple DLs situated both below and above E_F, the unique identification is even more complicated due to the interference of DL occupancy. The extensive data collection involving spectral and variable intensity measurements completed by detailed numerical simulation as presented in this paper is thus indispensable.

B. Shockley-Reed-Hall charge kinetic simulations

The Shockley-Read-Hall theory [48] complemented by an illumination-mediated deep level to band transitions, as shown in Fig. 3, is used to analyze two alternative DL models and NDPC appearance in detail. The evaluation of the corresponding charge dynamics is performed in the steady-state illumination regime. Equations (8)–(10) represent the

electron, hole, and DL occupancy dynamics:

$$\frac{\partial n}{\partial t} = -\sum_i U_i^e + \sum_i I_{ci} + I_{bb} - U_{bb}, \tag{8}$$

$$\frac{\partial p}{\partial t} = -\sum_i U_i^h + \sum_i I_{vi} + I_{bb} - U_{bb}, \tag{9}$$

$$\frac{\partial n_{ti}}{\partial t} = U_i^e - I_{ci} - U_i^h + I_{vi}, \tag{10}$$

$$U_i^e = \sigma_{ei} v_e [(N_{ti} - n_{ti})n - n_{ti}n_{1i}], \tag{11}$$

$$U_i^h = \sigma_{hi} v_h [n_{ti}p - (N_{ti} - n_{ti})p_{1i}], \tag{12}$$

$$I_{ci} = I\tilde{\alpha}_{ei}n_{ti}, \tag{13}$$

$$I_{vi} = I\tilde{\alpha}_{hi}(N_{ti} - n_{ti}), \tag{14}$$

$$I_{bb} = G_{bb}I, \tag{15}$$

$$U_{bb} = C_{bb}(np - n_i^2), \tag{16}$$

where n, p, n_{ti}, U_i^e (U_i^h), I_{bb}, and U_{bb} are the densities of free electrons, free holes, electrons trapped in the ith level, electron (hole) net recombination rate at the ith level, the interband light-induced generation rate, and the band-to-band net recombination rate, respectively. The quantities defining recombination rates n_i, N_{ti}, σ_{ei}, σ_{hi}, v_e, and v_h in Eqs. (10)–(14) are intrinsic carrier density, ith DL density, electron and hole thermal capture cross sections, and
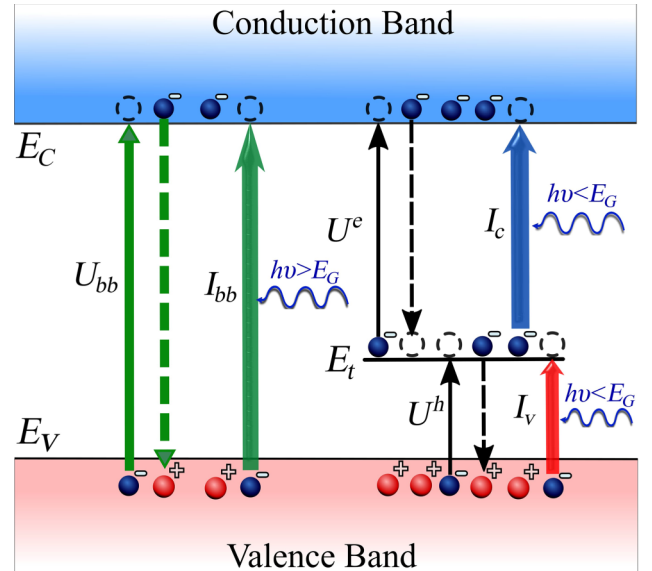

FIG. 3. Shockley-Read-Hall carrier generation-recombination model. Antiparallel solid and dashed arrows show thermal carrier generation and recombination processes (band-to-band or DL-assisted). Solid upward arrows correspond to photon-assisted free-carrier generation (band-to-band or DL-assisted).

electron (hole) thermal velocities, respectively. Symbols n_{1i} and p_{1i} stand for electron and hole densities in the case of the Fermi level E_F being set equal to the DL ionization energy E_{ti} [48]. The effect of illumination on the *i*th DL occupancy is defined by the I_{ci} (I_{vi}) generation rate from the *i*th level to the conduction (valence) band where I, $\tilde{\alpha}_{ei}$, and $\tilde{\alpha}_{hi}$ are the photon flux and photon capture cross sections relevant to the conduction and valence band transition, respectively. The interband light-induced generation rate I_{bb} can be neglected for $h\nu < E_g$. The band-to-band recombination constant $C_{bb} = 10^{-11}$ cm^2 can be estimated for Cd$_{1-x}$Mn$_x$Te according to Ref. [49]. The band-to-band recombination rate is typically much less in comparison with the DL-assisted recombination rate, and thus, can be neglected. The values of photon capture cross section are chosen to fit the shape of PHES spectra and the order of magnitude is chosen according to Ref. [17]. Both photon-energy and photon-flux dependencies are fitted simultaneously by the same parameters. The charge neutrality is assured by the neutrality equation:

$$p - n - \sum_i n_{ti} = p_0 - n_0 - \sum_i n_{t0i}, \qquad (17)$$

where the dark densities p_0, n_0, and n_{t0i} on the right-hand side are defined by the position of Fermi energy E_F. The solution of Eqs. (8)–(10) and (17) significantly simplifies in the steady-state regime, where the time derivatives are set to zero. The electron and hole lifetimes τ_e and τ_h can be found by the relations

$$\tau_e = \frac{1}{\sum_i v_{ei}\sigma_{ei}(N_{ti} - n_{ti})}, \qquad (18)$$

$$\tau_h = \frac{1}{\sum_i v_{hi}\sigma_{hi}n_{ti}}. \qquad (19)$$

The occupation of DLs can be conveniently described by a dimensionless filling factor (FF), which is defined as the ratio of DL electron occupation and the total DL concentration $f_i = n_{ti}/N_{ti}$. The change of the DL occupation from the equilibrium under illumination intensity I can be presented by reduced filling factor $F_i(I)$, $-1 < F_i < 1$:

$$F_i(I) = f_i(I) - f_i(0). \qquad (20)$$

The occupation and depletion of the deep level can be tracked by the positive or negative sign correspondingly.

IV. RESULTS AND DISCUSSION

A. Deep levels, carrier mobility, and negative differential photoconductivity

Photoconductivity and Hall mobility spectra measured in the energy range 0.6–1.8 eV under three different photon fluxes are presented in Fig. 4. One can see rises
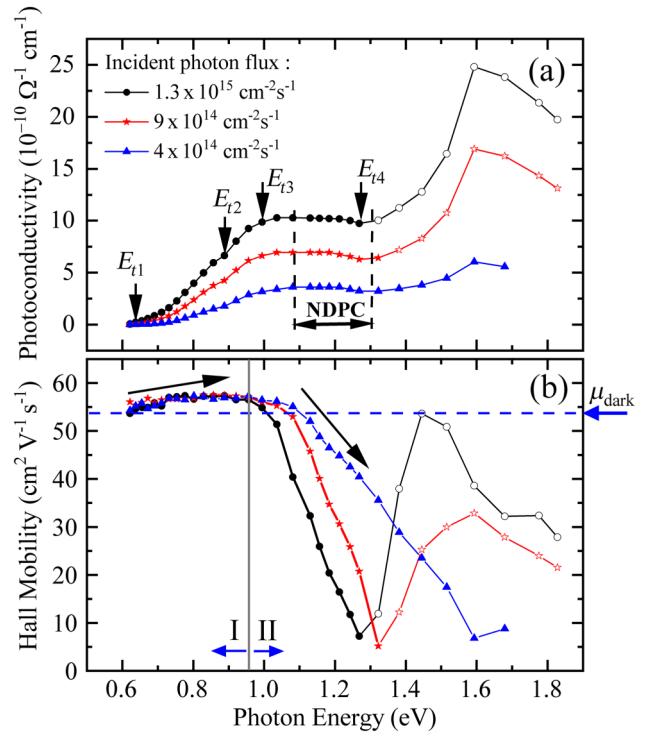

FIG. 4. (a) Photoconductivity and (b) Hall mobility spectra at different photon fluxes. Vertical arrows show the deep-level-threshold energy. Here and henceforth the points with the negative V_H sign are shown by empty symbols.

and the change of the PhC slope at 0.63, 0.9, 1.0, and 1.3 eV photon energies related to the presence of DLs near these threshold energies. It is important to note that PhC reveals a noticeable increase at the energy slightly above 0.6 eV. This result proves the existence of empty states at this energy localized relatively to E_V. We thus deduce that the position of E_F does not deviate markedly from $E_F = E_V + 0.62$ eV determined from the dark hole density and the effect of surface leakage current to the transport properties discussed in Sec. II B is low. Increasing further the excitation energy, PhC starts to saturate or even decreases in the energy region 0.96–1.3 eV, Fig. 4(a). This effect is known as the negative differential photoconductivity. The Hall mobility μ_H increases from 0.62 eV up to 0.96 eV where it starts to saturate, Fig. 4(b), Region I. The increase of μ_H in the *p*-type sample is reached by the free-hole generation according to Eq. (7) associated with the transitions to DLs from the valence band in this energy region as mentioned in Sec. III A. The μ_H decrease can be observed at $h\nu > 0.96$ eV, Region II, and the negative sign of V_H is reached near 1.3 eV for a maximal photon flux of 1.3×10^{15} cm^{-2} s^{-1}. The decrease of μ_H is caused by free electrons generated in this region. One can see that the sign change of μ_H depends on the illumination intensity being shifted to higher photon energy at decreasing photon flux 9×10^{14} cm^{-2} s^{-1} and 4×10^{14} cm^{-2} s^{-1}. In contrast

to the abrupt change of μ_H induced by photoelectrons, PhC remains stable in the energy region 1.0–1.4 eV, which proves the stable hole density dominating in *cond* and PhC. Once a negative sign of V_H is reached, μ_H increases with the further increase of the photon energy in agreement with Eq. (7).

To find the position of DL relative to E_C and E_V, i.e., to distinguish the level model 1 and 2 outlined in Fig. 2, free-carrier-concentration spectra are needed. For evaluation of n and p from Eqs. (6) and (7) in the mixed conductivity regime corresponding mobilities μ_e and μ_h must be known. The theoretically predicted values are often chosen in the photo Hall measurements in CdTe [6] and perovskites [12]. However, such a choice is not convenient for this analysis and it can lead to incorrect conclusions. The real value of mobility affected by actual free-carrier density must be measured directly. According to Eq. (7), electron and hole mobilities can be found in the conditions where only one type of carrier is dominating. As we already found, energy regions I and II, where photoexcited holes (with maximal hole mobility at approximately 0.96 eV), and electrons (with maximal electron effect at approximately 1.45 eV) dominate; μ_H is measured as a function of photon flux at these energies using laser diodes as an enhanced illumination source. We show in Fig. 5 the rapid increase of μ_H both for electrons in Fig. 5(a), where μ_H saturates at 925 ± 11 cm^2 s^{-1} V^{-1}, and for holes in Fig. 5(b) with saturation at 59.6 ± 0.4 cm^2 s^{-1} V^{-1}. In this paper, saturated values of the Hall mobility observed in Figs. 5(a) and 5(b) are further associated with free-carrier mobility.

Free electron and hole concentration spectra in the energy range 0.6–1.8 eV calculated from Eqs. (6) and (7) and data from Fig. 4 using saturation values of the Hall mobility are presented in Fig. 6. One can see the rise of hole concentration at the energies 0.63 and 0.9 eV. These changes of the spectra are associated with a photon-induced transition from the valence band to DLs with threshold energies $E_{t1} = E_V + 0.63$ eV, and $E_{t2} = E_V + 0.9$ eV. As seen from Fig. 6(b), no free-electron generation is detected in the energy region $h\nu < 0.96$ eV. Therefore, free electrons are neglected in region I. Corresponding transitions and DL-threshold energies are schematically shown in Fig. 7.

The rise of the electron concentration can be observed at 0.96 and 1.25 eV photon energies and is associated with electron transitions from the DLs localized below or close to the Fermi level with threshold energies $E_{t3} = E_C - 1.0$ eV and $E_{t4} = E_C - 1.3$ eV (taking into account the resolution of the output light), which are the subject of model 1 discussed further, or secondary transitions from alternative DLs $E_{t3} = E_V + 1.0$ eV and $E_{t4} = E_V + 1.3$ eV related to model 2. The rise of the electron concentration n is followed by saturation and decrease of the hole concentration p. In view of the fact that NDPC appears at similar photon energy where electrons start to operate, we deduce
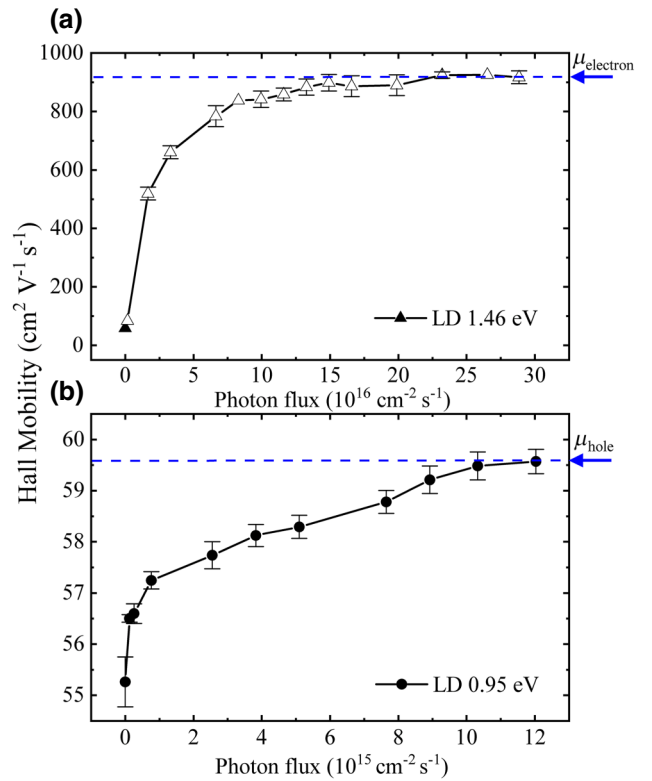

FIG. 5. Hall mobility measurements at extended photon fluxes with photon energies (a) 1.46 eV and (b) 0.95 eV. Horizontal arrows and dashed lines show saturation values of the Hall mobility associated with electron and hole mobility. Solid and empty symbols represent data with the positive and negative sign of V_H.

that principal recombination level responsible for electron-hole recombination rules the process. The PhC decrease in this region is damped by the free-electron rise in the NDPC region. It is important to note that DL-threshold energies can be mistakenly shifted at lower-illumination photon fluxes and such tendency can be seen in Fig. 6(b) near 1.0 eV photon energy. The conventional light sources [18] often used with a monochromator have maximal output photon flux of 10^{14} cm^{-2} s^{-1}. The electron concentration at photon fluxes less than 4×10^{14} cm^{-2} s^{-1} is nearly undetectable.

B. Deep-level detection and charge-carrier Shockley-Reed-Hall simulations

In this section, we introduce SRH simulation which represents the fit of all experimental data according to Eqs. (8)–(17) with parameters from Table I, denoted as model 1(a). Models 1(b) and 1(c) represent simulations where the variation of DL parameters takes place to see the influence of DL properties on the studied effects, see Table II. Model 2 is a simulation with alternative DL position above E_F mentioned above in Sec. IV A.

TABLE I.   Deep level parameters of model 1(a).

DL	E_{t1}	E_{t2}	E_{t3}	E_{t4}
Position in the bandgap, eV	$E_V + 0.63$	$E_V + 0.9$	$E_C - 1.0$	$E_C - 1.3$
N_t, cm^{-3}	10^{13}	6.5×10^{12}	3.5×10^{12}	8×10^{12}
σ_e, cm^2	3×10^{-17}	9×10^{-13}	5×10^{-14}	2×10^{-14}
σ_h, cm^2	4×10^{-16}	5×10^{-14}	5×10^{-13}	3×10^{-19}
n_{ti}/N_{ti}[a]	0.35	10^{-5}	0.49	1

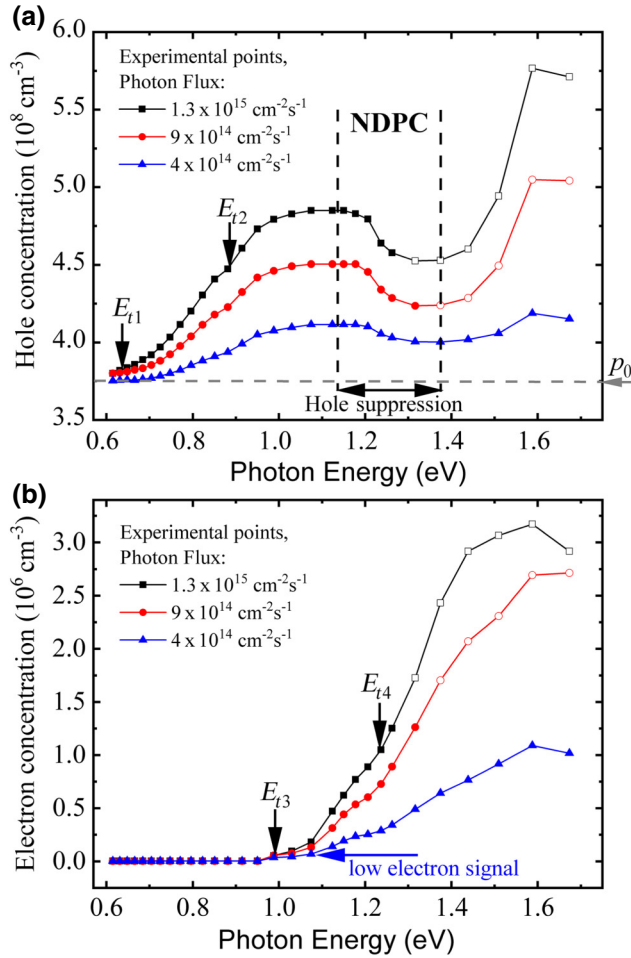[a]The relative deep-level occupation at equilibrium.

FIG. 6.   (a) Hole and (b) electron concentration spectra at different photon fluxes. Vertical arrows show DL-threshold energies. Vertical dashed lines separate the region of negative differential photoconductivity.

TABLE II.   Variation of deep-level parameters of model 1(a).

Model No.	Changed parameters
Model 1(b)	$\sigma_{h2,1(b)} = 10 \times \sigma_{h2} = 5 \times 10^{-13}$ cm^2
Model 1(c)	$N_{t2,1(c)} = 10 \times N_{t2,1(c)} = 6.5 \times 10^{13}$ cm^{-3}
Model 2	$E_{t3,(2)} = E_V + 1.0$ eV; $E_{t4,(2)} = E_V + 1.3$ eV

Concentrations of holes and electrons calculated according to Shockley-Reed-Hall model simulations completed by four DLs from model 1 and model 2 are shown in Fig. 8 by dashed and dashed-dotted lines, respectively. DL-threshold energies E_{t1} and E_{t2} are fixed in both models as these energies appear safe. The variation of the model parameters over a wide range according to the DL parameters in the literature [50,51] showed that competing model 2 fails to provide electron concentration $\Delta n > \Delta p$ in the region $hv > 1.0$ eV, because an emissionlike electron generation is followed by strong hole generation. Moreover, p decrease and NDPC are not reached for the same reason. The behavior of free holes and electrons in this region excludes the possibility of another DL localization in the bandgap (with $E_t > E_F$), where electron rise is produced by secondary electron generation. On the other hand, model 1 shows good results in simulation of the PHES spectra, see curve model 1(a) in Fig. 8. This proves the validity of the proposed PHES deep-level-detection concept. Note that DLs E_{t1}, E_{t2}, and E_{t3} have similar activation energies, which can hardly be resolved by photoluminescence
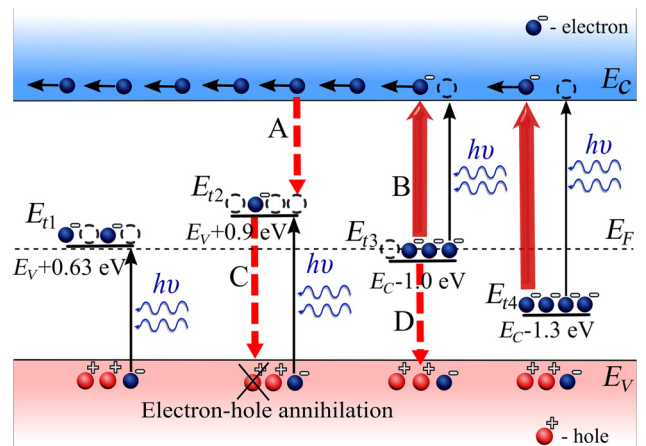

FIG. 7.   The defect model 1 with pondered transitions of the deep levels. Full upward black arrows delineate principal optical excitation. Bold and dashed red arrows show the generation-recombination traffic, which leads to fast electron-hole annihilation and decrease (saturation) of hole concentration under illumination.

or thermal activation methods where DL band overlapping occurs [16,18]. According to model 1(a) and Table I, the electron lifetime $\tau_e = 40$ ns is controlled by electron trap DL E_{t2} due to strong recombination. DL E_{t3} plays a minor role in the electron trapping due to lower concentration and electron capture cross section. The majority hole lifetime $\tau_h = 100$ ns is controlled mainly by the hole trap E_{t3}. A note should be given on the effect of possible deviation of E_F from the value $E_v + 0.62$ eV determined with the dark conductivity possibly violated by the surface conduction. For example, the 50 meV shift of E_F further from E_V leads in a fit with two-times larger concentration of DLs E_{t1} and E_{t3} situated near E_F. Properties of other DLs remain unaffected.
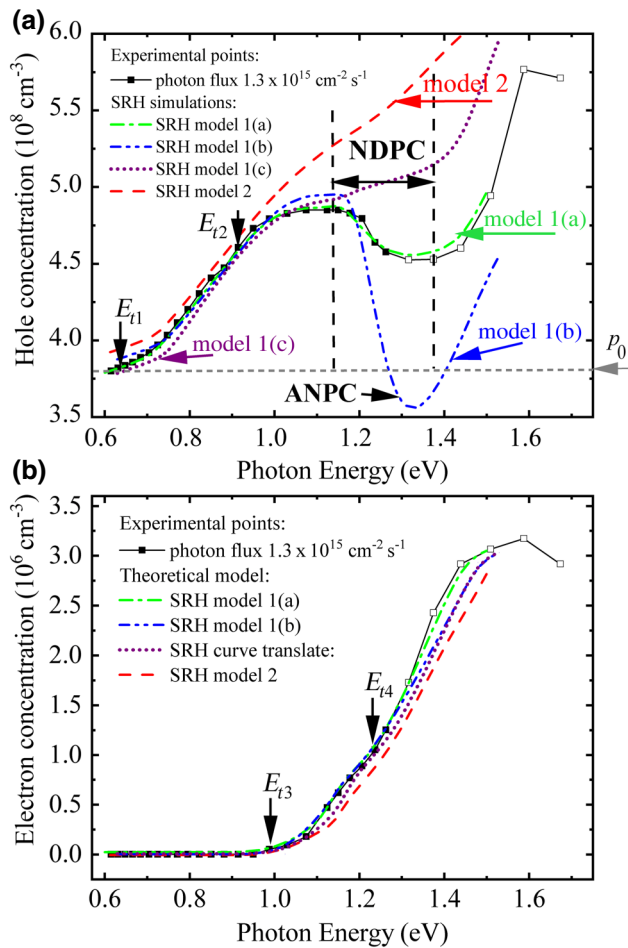

FIG. 8. Dashed (dashed-dotted) curves show SRH model simulations for two possible models [model 1(a) and model 2]. Models 1(b) and 1(c) show SRH simulation in the case of increased capture cross section and defect concentration of the recombination DL, respectively. Theoretical curves are calculated for the maximum photon flux and linearly shifted upwards or downwards with an increment of 1% for better visualization. The solid line with squares shows experimental data from Fig. 6 for the maximum photon flux.

C. Negative differential photoconductivity characterization

According to experimental results and SRH simulations, the electron generation in region II is provided by DLs E_{t3} and E_{t4} localized below E_F (model 1, Fig. 7) and the hole concentration rises are induced by DLs E_{t1}, and E_{t2}. According to model 1(a), the effect of NDPC detected in Fig. 4(a) is produced by the decrease of the hole concentration confirmed in the experiment, Fig. 6(a). The decrease of the majority carrier's concentration under subbandgap illumination is reached by minority carrier's fast recombination supported mainly by DL E_{t2} and as a result of electron-hole annihilation, as shown in Fig. 7 by bold and dashed red arrows (processes A–D). DL E_{t2} is empty enough to provide a strong recombination channel for free electrons. The decrease of hole and increase of electron concentrations match the experimental points in the NDPC region and confirm the reliability of the proposed deep-level-assisted NDPC model.

For further calculation, we chose trap E_{t2} as the most important recombination channel to show the dependence of the main NDPC effects on DL parameters. Other DLs are occupied and have insufficiently low carrier capture cross sections. Therefore, they can hardly serve as a strong recombination channel. The effect of hole concentration decrease associated with NDPC depends on the capture cross section σ_{h2}, which represents the hole recombination rate of the DL, see Eq. (12). The curve of model 1(a), in Fig. 8, shows results for $\sigma_{h2} = 5 \times 10^{-14}$ cm^2 and model 1(b) represents simulation, where $\sigma_{h2,1(b)} = 5 \times 10^{-13}$ cm^2. The hole concentration decrease can be stimulated even more expressively and the concentration $p < p_0$ can be reached by the σ_{h2} increase. A similar effect can be produced by electron photogeneration [$\sim I\tilde{\alpha}_{ei}$ in Eq. (13)] increase from the DLs E_{t1}, E_{t3}, or E_{t4}. The effect of the carrier decrease under illumination below the dark equilibrium values is known as absolute negative photoconductivity. We found that the decrease in the hole concentration in the NDPC region is not observed for capture cross sections $\sigma_{h2} < 2 \times 10^{-14}$ cm^2.

To show the effect of the recombination DL concentration on p decrease we developed model 1(c), where the concentration of the recombination channel DL E_{t2} (2×10^{13} cm^{-3}) is higher by an order of magnitude than in model 1(a) (6.5×10^{12} cm^{-3}), see spectra in Fig. 8 (dotted purple line). Despite the fact that electron lifetime is dropped from the value 40 to 4 ns, the decrease of p in the NDPC region is completely suppressed. The main reason for this result is comprised in the increase of DL E_{t2} concentration, which also implies an increase of the terms $\sigma_{hi}\nu_h(N_{ti} - n_{ti})p_{1i}$ and $I\tilde{\alpha}_{hi}(N_{ti} - n_{ti})$ responsible for the thermal and optical generation of free holes, see Eqs. (9), (12), and (14). Meanwhile, the recombination term $\sigma_{hi}\nu_h n_{ti}p$ and electron generation term $I_{ei} = I\tilde{\alpha}_{ei}n_{ti}$

are increasing slowly due to the emptiness of the DL above E_F. That is why the free-hole concentration increases in the NDPC region and does not decrease when DL concentration increases. It is important to recall that the deep level E_{t3} acts as an alternative recombination channel in the case of the absence of the deep level E_{t2}. Therefore, to define the lower concentration of the recombination channel at which NDPC is observed, DL E_{t3} must be included for analysis. We find that the decrease of the hole concentration under illumination is observed when DL concentrations met the following relation

$$10^{10} \text{ cm}^{-3} < \frac{N_{t2} + N_{t3}}{2} < 2 \times 10^{13} \text{ cm}^{-3}. \quad (21)$$

As one can see, even in the material with relatively low defect concentration [5], NDPC can be stimulated. Multiplying the left part on the limit value for capture cross section we get the NDPC lower-limit rule for CdMnTe material.

$$N_t \sigma_h > 2 \times 10^{-4} \text{ cm}^{-1}. \quad (22)$$

It should be noted that in the case where electron generation channels are absent (DLs E_{t3} and E_{t4} localized below E_F), the NDPC effect vanishes, see Fig. 8(a) model 2. This illustrates an important fact that both recombination and minority carrier generation channels must be present in the material to observe negative differential photoconductivity effect.

D. Charge-carrier-transport simulations under high-illumination fluxes

The illumination either below or above bandgap energy is often used to study the detector performance instead of x- and gamma-ray or alpha-particle radiation sources [52,53]. The carrier concentrations of $Cd_{1-x}Mn_xTe$ are studied under extensive 1.46 eV laser illuminations, to show the influence of discovered DLs and NDPC on the

material absorption properties. One can see in Fig. 9 that the hole concentration starts to saturate and reaches the saturation value of 1.8×10^9 cm^{-3} at photon flux 7×10^{16} s^{-1} cm^{-2} in the $Cd_{1-x}Mn_xTe$ sample. The further increase of photon flux does not enhance the free-hole concentration. The suppression of p is followed by a slow super-linear increase of n. The proposed NDPC deep level, model 1(a), presented by a solid curve is in a good agreement with experimental data. Experimental data and SHR simulations with DL positions in the bandgap discovered by PHES show that such hole suppression and super-linear electron increase are the consequence of the recombination through half-empty DL E_{t2} (and partially DL E_{t3}) and further electron-hole annihilation. Numerical simulations also show that in the absence of the electron generation channel, according to model 2, no NDPC can be observed. In the case of an enhanced recombination channel, model 1(b), the appearance of NDPC effect is followed by ANPC at higher flux as predicted by the PHES spectra simulation, Fig. 8(a) NDPC region.

The occupancy of deep levels of model 1(a) as a function of photon flux is shown in Fig. 10 by means of reduced filling factor $F_i(I)$. The electron generation at 1.46 eV photon energy is supported by DLs E_{t1}, E_{t3}, and E_{t4}, as seen from the depletion of the corresponding DLs. The recombination of minority electrons is driven by DLs E_{t2} and E_{t3}, where the increased occupation of DLs is observed. Note the nontrivial occupation shape of DL E_{t3}. According to Eq. (8) the generation rate I_{ci} is connected to recombination rate U_i^e. With increasing illumination intensity both terms are increasing, see Eqs. (8) and (13). Due to the initial depletion tendency of DL E_{t3}, the electron thermal emission part of the net recombination rate $\sigma_{ei} v_e n_{ti} n_{1i}$ is decreasing in comparison to the equilibrium state. In contrast, the electron capture rate $\sigma_{ei} v_e (N_{ti} - n_{ti}) n$ is increasing and predominates the thermal emission part. Similar tendencies are observed for the hole-associated processes U_i^h and I_{vi}. Note that the electron-generation rate
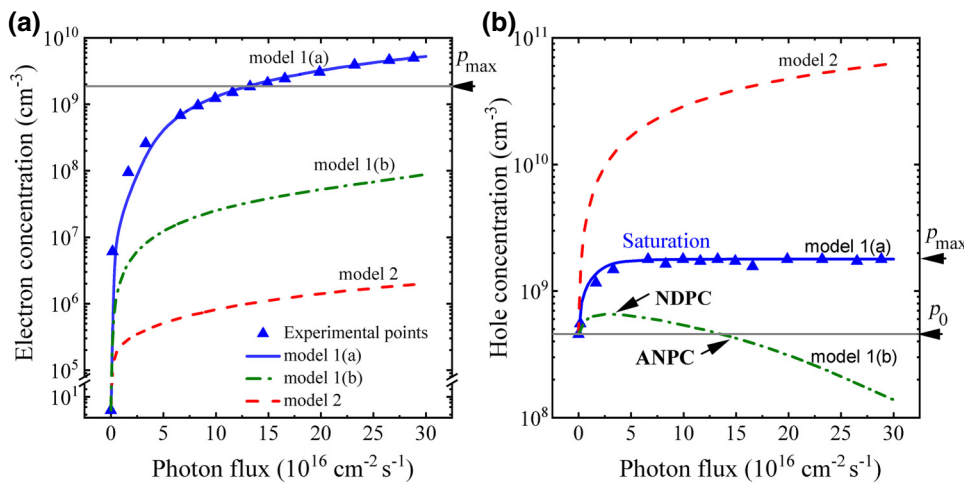

FIG. 9. (a) Electron and (b) hole concentration as a function of photon flux at 1.46 eV high-flux illumination in $Cd_{1-x}Mn_xTe$. Solid, dashed-dotted, and dashed curves show SRH simulations for model 1(a), model 1(b), and model 2.
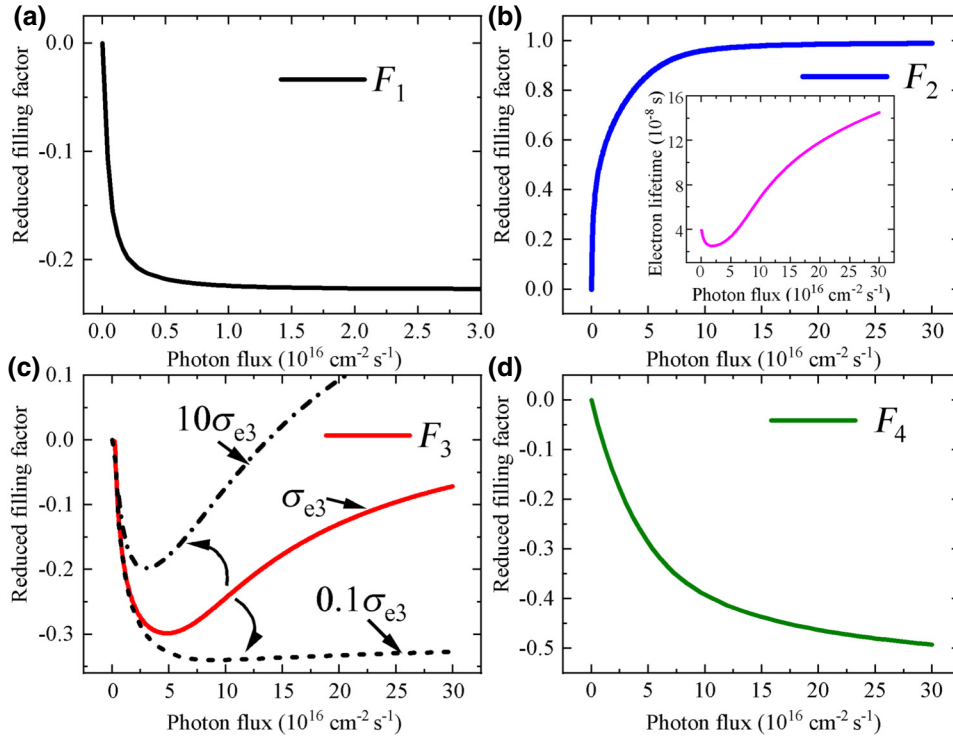
FIG. 10. Deep-level-reduced filling factor calculated by SRH theory for model 1(a) at 1.46 eV high-flux illumination with deep levels from Fig. 7. (a), (b), (c), and (d) Relative occupation of DLs with energies $E_{t1} = E_V + 0.63$ eV, $E_{t2} = E_V + 0.9$ eV, $E_{t3} = E_C - 1.0$ eV, and $E_{t4} = E_C - 1.3$ eV, respectively. The inset in Fig. 10(b) shows the electron lifetime as a function of the photon flux.

I_{ci} is proportional to n_{ti} and the hole-generation rate I_{vi} is proportional to $N_{ti} - n_{ti}$. Due to the initial tendency of electron depletion of partly filled DL, the hole-generation rate is increasing faster than the electron one. This synergy of facts leads to nontrivial DL E_{t3} occupation. To emphasize the influence of the electron recombination through DL E_{t3} on nontrivial occupation behavior (process A, Fig. 7), we present the occupancy profiles for enlarged and reduced electron capture cross section σ_{e3} in Fig. 10(c).

The charge-carrier lifetime of the majority carriers in inorganic semiconductors is controlled by recombination or traplike DLs with a high-capture cross section. According to SRH simulation for model 1(a), the electron lifetime depends on the illumination photon flux, and this dependence has complicated character, see the inset in Fig. 10(b). The value of τ_e decreases at relatively low photon flux up to 2.2×10^{15} cm^{-2} s^{-1} due to the activation of a new recombination channel as a result of the occupation depletion of DL E_{t3}, see Fig. 10(c) and Eq. (18). A further increase of the photo flux leads to the τ_e enhancement due to the increase of DL E_{t3} and DL E_{t2} occupation.

The understanding of complicated dynamics of the space charge in radiation detectors utilized at high flux has been a serious problem so far [40,54–57]. Both negative and positive space charge appearing at different excitation conditions [52] disturbs the charge transport due to activation of additional recombination channels and device polarization [5,58].

V. CONCLUSION

Photo-Hall-effect spectroscopy with enhanced illumination has proven a powerful tool for material characterization and deep-level detection. The enhanced illumination allows for a separate experimental investigation of both minority and majority carriers. Absolute positions of deep levels in the bandgap hardly accessible by conventional spectroscopy methods are determined by PHES.

The determination of the exact positions of DLs relatively to E_C and E_V detected by PHES is crucial for the material characterization. The data obtained from PHES are used for developing the charge generation-recombination model. We show that such a model is very useful for a detailed analysis and understanding of effects like negative differential photoconductivity, absolute negative photoconductivity, etc. These multiple benefits and the resolved problem of DL energy detection place photo-Hall-effect measurements with enhanced monochromatic illumination over other material characterization methods.

We explain the appearance of negative differential photoconductivity by fast-minority carrier recombination through the nearly empty DLs and subsequent electron-hole annihilation, which leads to a decrease or saturation of majority carrier concentration. The importance of parallel activity of both recombination and generation channels to observe NDPC is demonstrated. We also present a comprehensive analysis of NDPC effect by means of SRH

simulations. We show the dependence of the effect on DL parameters such as carrier-capture cross sections and DL concentration, as well as the connection between negative differential photoconductivity and absolute negative photoconductivity. The influence of such an effect on the material properties is studied in the regime of enhanced laser illumination at $hv = 1.46$ eV. It is argued that the appearance of NDPC depreciates charge-transient properties and leads to undesirable loss of photocarriers. NDPC can be observed even in a material with relatively low defect concentration. It is also shown that the proper light illumination can be used for the improvement of the free-carrier lifetime in semiconductors.

ACKNOWLEDGMENTS

[1] A. Castaldini, A. Cavallini, B. Fraboni, P. Fernandez, and J. Piqueras, Deep energy levels in CdTe and CdZnTe, J. Appl. Phys. **83**, 2121 (1998).

[2] J. Zazvorka, P. Hlidek, R. Grill, J. Franc, and E. Belas, Photoluminescence of CdTe:In the spectral range around 1.1 eV, J. Lumin. **177**, 71 (2016).

[3] J. Franc, P. Hlídek, E. Belas, V. Linhart, S. Pospíšil, and R. Grill, Photoconductivity spectroscopy of deep levels in CdTe, IEEE Trans. Nucl. Sci. **52**, 1956 (2005).

[4] A. Carvalho, A. K. Tagantsev, S. Öberg, P. R. Briddon, and N. Setter, Cation-site intrinsic defects in Zn-doped CdTe, Phys. Rev. B **81**, 075215 (2010).

[5] A. Musiienko, R. Grill, J. Pekárek, E. Belas, P. Praus, J. Pipek, V. Dědič, and H. Elhadidy, Characterization of polarizing semiconductor radiation detectors by laser-induced transient currents, Appl. Phys. Lett. **111**, 082103 (2017).

[6] J. Rosenzweig, Bipolar photo-Hall effect in CdTe, J. Cryst. Growth **59**, 263 (1982).

[7] F. J. Bartoli, Characterization of impurities in p-type HgCdTe by photo-Hall techniques, J. Vac. Sci. Technol. A Vac. Surf. Films **4**, 2047 (1986).

[8] P. Hubik, J. J. Mares, J. Kristofik, A. Baraldi, C. Ghezzi, and A. Parisini, Hall and photo-Hall effect measurements on sulphur-doped GaSb, Semicond. Sci. Technol. **10**, 455 (1995).

[9] R. Ascázubi, C. Shneider, I. Wilke, R. Pino, and P. S. Dutta, Enhanced terahertz emission from impurity compensated GaSb, Phys. Rev. B - Condens. Matter Mater. Phys. **72**, 045328 (2005).

[10] K. Yasutake, H. Kakiuchi, A. Takeuchi, K. Yoshii, and H. Kawabe, Deep-level characterization in semi-insulating GaAs by photo-induced current and Hall effect transient spectroscopy, J. Mater. Sci. Mater. Electron. **8**, 239 (1997).

[11] K. C. Lin, M. Y. Li, D. C. Ling, C. C. Chi, and J. C. Chen, Evolution of hot carrier dynamics in graphene with the Fermi level tuned across the Dirac point, Phys. Rev. B **91**, 125440 (2015).

[12] Y. Chen, H. T. Yi, X. Wu, R. Haroldson, Y. N. Gartstein, Y. I. Rodionov, K. S. Tikhonov, A. Zakhidov, X. Y. Zhu, and V. Podzorov, Extended carrier lifetimes and diffusion in hybrid perovskites revealed by Hall effect and photoconductivity measurements, Nat. Commun. **7**, 12253 (2016).

[13] Y. Chen, H. T. Yi, and V. Podzorov, High-Resolution ac Measurements of the Hall Effect in Organic Field-Effect Transistors, Phys. Rev. Appl. **5**, 034008 (2016).

[14] H. T. Yi, Y. N. Gartstein, and V. Podzorov, Charge carrier coherence and Hall effect in organic semiconductors, Sci. Rep. **6**, 23650 (2016).

[15] J. Kubat, H. Elhadidy, J. Franc, R. Grill, E. Belas, P. Hoschl, and P. Praus, Evaluation of the concentration of deep levels in semi-insulating CdTe by photoconductivity and TEES, IEEE Trans. Nucl. Sci. **56**, 1706 (2009).

[16] R. Grill, J. Franc, H. Elhadidy, E. Belas, Š. Uxa, M. Bugár, P. Moravec, and P. Höschl, Theory of deep level spectroscopy in semi-insulating CdTe, IEEE Trans. Nucl. Sci. **59**, 2383 (2012).

[17] A. Musiienko, R. Grill, P. Moravec, G. Korcsmáros, M. Rejhon, J. Pekárek, H. Elhadidy, L. Šedivý, and I. Vasylchenko, Dual-wavelength photo-Hall effect spectroscopy of deep levels in high resistive (CdZn) Te with negative differential photoconductivity, J. Appl. Phys. **123**, 161502 (2018).

[18] A. Musiienko, R. Grill, P. Hlidek, P. Moravec, E. Belas, J. Zázvorka, G. Korcsmáros, J. Franc, and I. Vasylchenko, Deep levels in high resistive CdTe and CdZnTe explored by photo-Hall effect and photoluminescence spectroscopy, Semicond. Sci. Technol. **32**, 015002 (2017).

[19] H. J. Stocker, Total Negative Photoconductance in Solids and Possibility of a New Type of Instability, Phys. Rev. Lett. **18**, 1197 (1967).

[20] M. Liao, Y. Koide, J. Alvarez, M. Imura, and J. P. Kleider, Persistent positive and transient absolute negative photoconductivity observed in diamond photodetectors, Phys. Rev. B **78**, 045112 (2008).

[21] B. Y. Sun and M. W. Wu, Negative differential transmission in graphene, Phys. Rev. B - Condens. Matter Mater. Phys. **88**, 235422 (2013).

[22] M. A. Mangold, M. Calame, M. Mayor, and A. W. Holleitner, Negative differential photoconductance in gold nanoparticle arrays in the Coulomb blockade regime, ACS Nano **6**, 4181 (2012).

[23] A. I. Yakimov, A. V. Dvurechenskii, A. I. Nikiforov, O. P. Pchelyakov, and A. V. Nenashev, Evidence for a negative interband photoconductivity in arrays of Ge/Si type-II quantum dots, Phys. Rev. B **62**, R16283 (2000).

[24] R. Labouvie, B. Santra, S. Heun, S. Wimberger, and H. Ott, Negative Differential Conductivity in an Interacting Quantum Gas, Phys. Rev. Lett. **115**, 050601 (2015).

[25] I. Shalish, C. E. M. de Oliveira, Y. Shapira, and J. Salzman, Hall photovoltage deep-level spectroscopy of GaN films, Phys. Rev. B **64**, 205313 (2001).

[26] F. Stockmann, Negative Photoeffekte in Haibleitern, Zeltschrift Fur Phys. **356**, 143 (1955).

[27] M. A. Jafarov, E. F. Nasirov, and S. A. Mamedova, Negative photoconductivity in films of alloys of II-VI compounds, Semiconductors **48,** 570 (2014).

[28] C. H. Lui, A. J. Frenzel, D. V. Pilon, Y. H. Lee, X. Ling, G. M. Akselrod, J. Kong, and N. Gedik, Trion-Induced Negative Photoconductivity in Monolayer MoS2, Phys. Rev. Lett. **113,** 166801 (2014).

[29] B. K. Ridley, A mechanism for negative differential resistance in III-V and II-VI semiconductors associated with the enhanced radiative capture of hot electrons, J. Phys. C Solid State Phys. **7,** 1169 (1974).

[30] R. H. Bube, Interpretation of Hall and photo-Hall effects in inhomogeneous materials, Appl. Phys. Lett. **13,** 136 (1968).

[31] T. Takahashi and S. Watanabe, Recent progress in CdTe and CdZnTe detectors, IEEE Trans. Nucl. Sci. **48,** 950 (2001).

[32] Q. Le Huy, J. L. Ducote, and S. Molloi, Radiation dose reduction using a CdZnTe-based computed tomography system: Comparison to flat-panel detectors, Med. Phys. **37,** 1225 (2010).

[33] H. A. Mohamed, Dependence of efficiency of thin-film CdS/CdTe solar cell on optical and recombination losses, J. Appl. Phys. **113,** 093105 (2013).

[34] E. Belas, S. Uxa, R. Grill, P. Hlídek, L. Šedivý, and M. Bugár, High temperature optical absorption edge of CdTe single crystal, J. Appl. Phys. **116,** 103521 (2014).

[35] E. Kamieniecki, Effect of charge trapping on effective carrier lifetime in compound semiconductors: High resistivity CdZnTe, J. Appl. Phys. **116,** 193702 (2014).

[36] J. Zhang, W. Jie, L. Luan, T. Wang, and D. Zeng, Evaluation of Mn uniformity in CdMnTe crystal grown by the vertical Bridgman method, J. Electron. Mater. **37,** 1158 (2008).

[37] U. N. Roy, A. E. Bolotnikov, G. S. Camarda, Y. Cui, A. Hossain, K. Lee, W. Lee, R. Tappero, G. Yang, R. Gul, and R. B. James, High compositional homogeneity of $CdTe_xSe_{1-x}$ crystals grown by the Bridgman method, APL Mater. **3,** 026102 (2015).

[38] K. H. Kim, A. E. Bolotnikov, G. S. Camarda, G. Yang, A. Hossain, Y. Cui, R. B. James, J. Hong, and S. U. Kim, Energy-gap dependence on the Mn mole fraction and temperature in CdMnTe crystal, J. Appl. Phys. **106,** 023706 (2009).

[39] K. H. Kim, G. S. Camarda, A. E. Bolotnikov, R. B. James, J. Hong, and S. Kim, Improved carrier-transport properties of passivated CdMnTe crystals, J. Appl. Phys. **105,** 093705 (2009).

[40] D. S. Bale and C. Szeles, Nature of polarization in wide-bandgap semiconductor detectors under high-flux irradiation: Application to semi-insulating $Cd_{1-x}Zn_x$ Te, Phys. Rev. B **77,** 035205 (2008).

[41] H. Elhadidy, V. Dedic, J. Franc, and R. Grill, Study of polarization phenomena in n-type CdZnTe, J. Phys. D. Appl. Phys. **47,** 055104 (2014).

[42] A. Hossain, A. E. Bolotnikov, G. S. Camarda, Y. Cui, D. Jones, J. Hall, K. H. Kim, J. Mwathi, X. Tong, G. Yang, and R. B. James, Novel approach to surface processing for improving the efficiency of CdZnTe detectors, J. Electron. Mater. **43,** 2771 (2014).

[43] S. U. Egarievwe, A. Hossain, I. O. Okwechime, R. Gul, and R. B. James, Effects of chemomechanical polishing on CdZnTe X-ray and gamma-ray detectors, J. Electron. Mater. **44,** 3194 (2015).

[44] N. Zambelli, G. Benassi, E. Gombia, M. Zanichelli, and D. Calestani, Electroless gold patterning of CdZnTe crystals for radiation detection by scanning pipette technique, Cryst. Res. Technol. **49,** 535 (2014).

[45] M. Prokesch and C. Szeles, Accurate measurement of electrical bulk resistivity and surface leakage of CdZnTe radiation detector crystals, J. Appl. Phys. **100,** 014503 (2006).

[46] K. Seeger, *Semiconductor Physics* (Springer-Verlag, Wien, 1973).

[47] COMPACT SUPERCONTINUUM LASER, http://www. Nktphotonics.Com/Lasers-Fibers/En/Product/Superk-Compact-Supercontinuum-Lasers/ (2017).

[48] M. Borgwardt, P. Sippel, R. Eichberger, M. P. Semtsiv, W. T. Masselink, and K. Schwarzburg, Excitation correlation photoluminescence in the presence of Shockley-Read-Hall recombination, J. Appl. Phys. **117,** 215702 (2015).

[49] W. Van Roosbroeck and W. Shockley, Photon-radiative recombination of electrons and holes in germanium, Phys. Rev. **94,** 1558 (1954).

[50] K. H. Kim, A. E. Bolotinikov, G. S. Camarda, A. Hossain, R. Gul, G. Yang, Y. Cui, J. Prochazka, J. Franc, J. Hong, and R. B. James, Defect levels of semi-insulating CdMnTe:In crystals, J. Appl. Phys. **109,** 113715 (2011).

[51] K. Kim, G. Jeng, P. Kim, J. Choi, A. E. Bolotnikov, G. S. Camarda, and R. B. James, Influence of the cooling scheme on the performance and presence of carrier traps for CdMnTe detectors, J. Appl. Phys. **114,** 063706 (2013).

[52] A. Cola and I. Farella, CdTe x-ray detectors under strong optical irradiation, Appl. Phys. Lett. **105,** 203501 (2014).

[53] K. Suzuki, T. Sawada, and S. Seto, Temperature-dependent measurements of time-of-flight current waveforms in Schottky CdTe detectors, IEEE Trans. Nucl. Sci. **60,** 2840 (2013).

[54] L. Abbene, G. Gerardi, and F. Principato, Digital performance improvements of a CdTe pixel detector for high flux energy-resolved x-ray imaging, Nucl. Instrum. Methods Phys. Res. A **777,** 54 (2015).

[55] D. S. Bale and C. Szeles, Electron transport and charge induction in cadmium zinc telluride detectors with space charge build up under intense x-ray irradiation, J. Appl. Phys. **107,** 114512 (2010).

[56] A. Santi, M. Zanichelli, G. Piacentini, M. Pavesi, A. Cola, and I. Farella, An original method to evaluate the transport parameters and reconstruct the electric field in solid-state photodetectors, Appl. Phys. Lett. **104,** 193503 (2014).

[57] M. Strassburg, C. Schroeter, and P. Hackenschmied, CdTe/CZT under high flux irradiation, J. Instrum. **6,** C01055 (2011).

[58] V. Dědič, M. Rejhon, J. Franc, A. Musiienko, and R. Grill, Space charge oscillations in semiinsulating CdZnTe, Appl. Phys. Lett. **111,** 102104 (2017).

Correction: Conversion errors in Eq. (6) have been fixed.